Plasma Physics and Controlled Fusion



OPEN ACCESS

RECEIVED
1 October 2025

REVISED
5 January 2026

ACCEPTED FOR PUBLICATION
4 February 2026

PUBLISHED
27 February 2026



PAPER

# Diagnostic x-ray source using electrons produced by a 100 J-class picosecond laser*

**Mitchell Sinclair[1,**], Isabella Pagano[2,3], Nuno Lemos[3], Charles D Arrowsmith[4,5], Jessica L Shaw[6], Kyle G Miller[6], Paul M King[2,3], Adeola Aghedo[3,7], Kenneth A Marsh[1], Gianluca Gregori[4], Félicie Albert[3,8] and Chan Joshi[1,8]**

[1] University of California, Los Angeles, CA, United States of America
[2] University of Texas at Austin, Austin, TX, United States of America
[3] Lawrence Livermore National Laboratory, Livermore, CA, United States of America
[4] University of Oxford, Oxford, United Kingdom
[5] Laboratory for Laser Energetics, Rochester, NY, United States of America
[6] University of Rochester, Laboratory for Laser Energetics, Rochester, NY, United States of America
[7] Florida A&M University, Tallahassee, FL, United States of America
[8] These authors jointly supervised this work.

* Omega EP operations, and support staff as without their work and dedication, such experimental research would not be possible.

**Author to whom any correspondence should be addressed.

**E-mail:** mdsinclair@ucla.edu

**Keywords:** hard x-ray source, laser plasma accelerator, backlighter

## Abstract

Many laser-based high-energy-density science (HEDS) facilities have one or more short-pulse (sub- to few-picosecond) laser beams for diagnostics. For the past decade, we have been developing a novel x-ray probing capability using such picosecond lasers interacting with an underdense plasma to produce relativistic electrons. The ultimate goal of these experiments is to demonstrate a new type of x-ray backlighter using the short-pulse ARC laser at the National Ignition Facility (NIF). Before this diagnostic is fielded at the NIF, it is critical to demonstrate the viability and reproducibility of the x-ray source on comparable high-power short-pulse laser systems. We present experiments that were carried out with the OMEGA EP laser at the University of Rochester's laboratory for laser energetics. In these experiments, high-energy electrons are produced through a combination of the self-modulation instability and direct laser acceleration in an underdense gas jet. These electrons generate directional x-rays with characteristic energies up to several tens of keV as they execute betatron motion in the ion channel, and the inverse Compton scattering process generates even harder x-rays, with characteristic photon energies of 60–240 keV. When implemented on the OMEGA EP laser(s), this x-ray source yields results that are comparable to those obtained recently on the short-pulse Titan laser at the Jupiter Laser Facility at Lawrence Livermore National Laboratory, after accounting for differences in laser energy, peak intensity, focusing $f/\#$, and plasma source. Applications of such an x-ray source for HEDS experiments are discussed.

## 1. Introduction

X-ray backlighting is a critical diagnostic tool in high-energy-density science (HEDS) experiments, particularly for radiographing hydrodynamic instabilities [1], implosion symmetry [2], and stagnation dynamics in inertial confinement fusion (ICF) targets [3]. Conventional laser-produced x-ray sources include recombination line radiation from solid targets embedded with highly ionized impurity atoms, as well as inner-shell $K_{\alpha,\beta}$ emission induced by hot electrons, or by radiation pumping. These sources are often limited in HEDS applications because of their relatively low photon energy, low flux, long duration, and large source sizes [3].

Over the past decade, our collaboration has been developing an x-ray source using relativistic (>100 MeV) electrons generated by a picosecond-class, 100 TW laser propagating through an underdense plasma [4, 5]. When relativistic electrons ($\gamma > 1$) are bent by the focusing force of a periodic magnetic field (undulator motion), bent by the transverse electric field of an ion column in a plasma (betatron motion) [6], decelerated by strong deflection from atomic nuclei (bremsstrahlung) [7, 8], or collide with an intense laser pulse (inverse Compton scattering) [9, 10], they emit radiation that is typically temporally incoherent but highly directional. Therefore, such a photon source can, in principle, be placed as far as 5–10 cm from the experimental package.

Early efforts in this field focused on betatron x-ray generation from laser-plasma accelerators [4]. However, it soon became apparent that many HEDS facilities worldwide-multi-beam, multi-kJ, 1–10 ns-class laser systems-also provide one or more picosecond short pulse beams. This realization redirected our work toward characterizing x-rays generated by picosecond relativistic laser-plasma interactions [11].

The initial years of our work were devoted to elucidating the mechanisms underlying electron acceleration in this regime [12]. The stimulated Raman forward scattering instability [13] and its multi-dimensional analog, the self-modulation instability (SMI), are known to generate relativistic plasma waves capable of trapping and accelerating a copious number of plasma electrons [14–16]. Experimental campaigns by our group and others show that when a picosecond-long, multi-TW laser pulse propagates through plasma with a typical density of 0.05–0.1 times the critical density $n_c$, the laser power quickly exceeds the critical power for self-focusing, and electron cavitation ensues [17–19]. The partially formed plasma channel guides the laser pulse and facilitates the excitation of a relativistic plasma wave. The longitudinal field of this plasma wave accelerates electrons to high energies, as shown in figure 1. The ion channel that remains in the plasma can also provide further direct acceleration of electrons by coupling to the transverse electric field of the laser-hence the term direct laser acceleration (DLA) [20, 21].

Betatron radiation arises when relativistic electrons accelerated in the plasma cavity undergo transverse oscillations driven by the focusing fields of the ion channel, producing synchrotron-like x-rays with a broadband spectrum [22, 23]. This radiation is emitted primarily in the forward direction from a micrometer-scale source, with photon energies extending up to tens of keV [4, 5, 24, 25]. In addition, even higher-energy x-rays can be generated not only within the underdense plasma itself, but also externally through inverse Compton scattering (ICS) [9] and bremsstrahlung mechanisms [26], using foils of variable thickness and material composition. In this work, we investigated how the addition of ICS increases the total forward hard-x-ray yield and maximum photon energy, noting that the electron beam-bremsstrahlung interaction with the low-$Z$ foil is negligible when compared to the ICS process. To realize ICS in a compact, single-beam geometry, we employed a 100 $\mu$m low-$Z$ (CH-plastic) foil as a plasma mirror that retro-reflects the drive pulse for a head-on interaction with the accelerated electron beam.

This work represents the first demonstration of a compact, directional hard x-ray source driven by picosecond laser-plasma interactions on a facility other than the Titan Laser at the Jupiter Laser Facility-specifically on OMEGA-EP at LLE-showing that the platform is reproducible, robust, and transferable across major HED facilities. We demonstrate betatron radiation, which provides a stable broadband flux up to tens of keV at $\sim 10^{10}$ ph keV sr$^{-1}$ [4, 5, 24, 25], along with ICS emission extending to 60–240 keV [9, 10], and (potentially) bremsstrahlung reaching energies above 1 MeV [7, 27]. Together, these mechanisms establish a tunable, point-projection backlighter that spans the 10–50 keV band for phase-contrast and low-$Z$ interface imaging, while providing higher-energy capability for shock, instability, and implosion diagnostics [28–31].

### 1.1. Particle-in-simulations of this directional hard x-ray source

Particle-in-cell (PIC) simulations using the 2D-OSIRIS [33] code illustrate the essential physics of relativistic picosecond laser–plasma interactions in underdense targets figure 1. A nominally 700 fs (FWHM) laser pulse with normalized vector potential $a_0 = 3$, with a ratio of peak power to critical power for relativistic self-focusing $P/P_c = 23$, and wavelength $\lambda = 1053$ nm propagates 1 mm into a fully ionized helium plasma of density $n_e = 1.0 \times 10^{19}$ cm$^{-3}$ ($n_e/n_c = 1\%$). Figure 1 summarizes the laser-plasma dynamics in a plasma window from 500 to 1000 $\mu$m: (a) after the laser pulse has propagated through approximately 1 mm of plasma, the rising edge of its envelope exhibits strong relativistic self-focusing with transverse compression of the $E_2$ field around $x_1 = 830$–$850$ $\mu$m; (b) the SMI develops rapidly, as indicated by the formation of nonlinear plasma waves behind the self-focused front, with the strongest longitudinal plasma wave annotated in green; (c) the electron density shows modulations associated with SMI, as well as electron bunching and partial channel formation between $x_1 = 615$–$915$ $\mu$m; and (d) the corresponding ion density profile reveals the developing ion channel, whose focusing force supports DLA and betatron x-ray emission. The region between the dashed lines in panels (c) and (d)

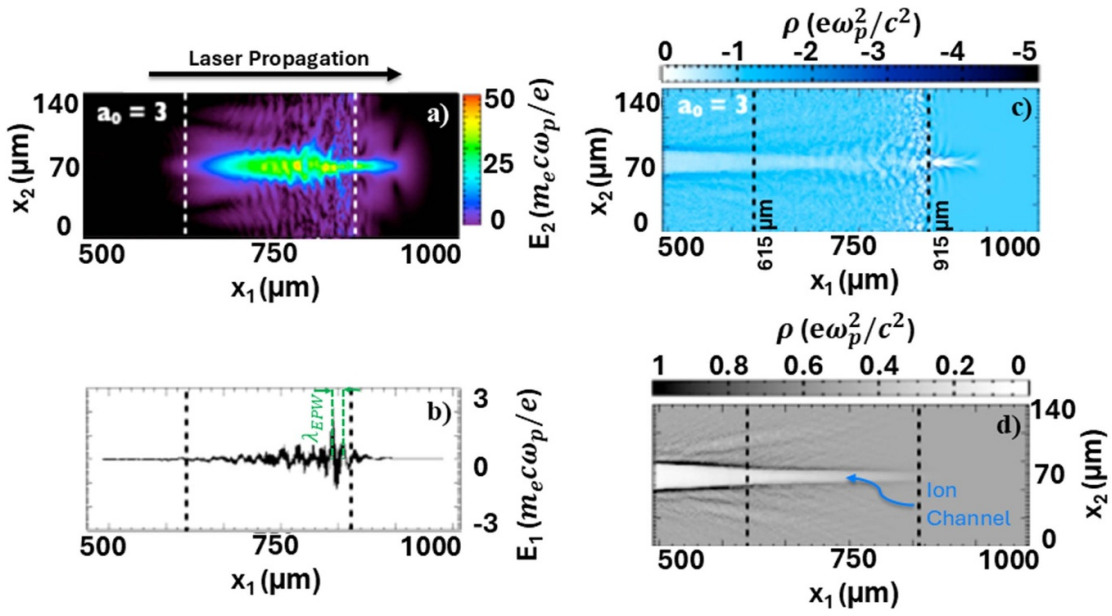


**Figure 1.** OSIRIS 2D particle-in-cell simulations of a relativistic ($a_0 = 3$, $\tau = 700$ fs) laser pulse after 1 mm of propagation in underdense helium plasma ($n_e = 1.0 \times 10^{19}\,\mathrm{cm}^{-3}$). (a) Envelope of the transverse (laser) electric field ($E_2$), (b) on-axis longitudinal electric field ($E_1$), (c) electron density, and (d) ion density. (a)–(d) Reproduced from [32]. 

marks the ion-channel region that predominantly contains the trapped electron population. Collectively, these simulations illustrate where the coupled action of SMI, DLA, and ion-channel–assisted DLA occur that produce electron beams with orders of magnitude higher charge—though at somewhat lower gradients, because of beam loading, and broader spectra—than in the ideal blowout regime of laser wakefield acceleration induced by an ultrashort laser pulse.

## 2. Experimental method

The experiments were carried out on OMEGA EP at the University of Rochester's laboratory for laser energetics (LLE) using a 100 J-class, short-pulse (∼1 ps) laser, making it an ideal platform for making a direct comparison with prior work carried out on the Titan Laser at JLF at LLNL [5, 17]. The electron beam characteristics of this platform on OMEGA EP have been published in detail elsewhere [34], but here we give an overview to set the stage for discussing the x-ray capabilities in the 10–100 keV photon energy range.

For repeatable and stable operation, we use a gas jet and a fast-acting valve system, which for OMEGA EP is capable of opening and closing within approximately 100 μs [35]. For these campaigns, a Mach 5 nozzle with a 6 mm opening (except for one experimental shot, taken with a 10 mm nozzle opening) was employed to spray a plume of helium gas, which the laser ionized to generate relativistic laser-plasma interactions, as described above, where these interactions are driven at approximately 1.8 mm above (Mach 5, 6 mm opening) or 2.7 mm above (Mach 5, 10 mm opening) the nozzle within a stable plasma density plateau that is adjustable from $1.5 \times 10^{18}\,\mathrm{cm}^{-3}$ to $5 \times 10^{19}\,\mathrm{cm}^{-3}$ [36].

The OMEGA EP laser system operates at a central wavelength of 1054 nm with a pulse duration of $700 \pm 100$ fs, with a typical shot rate of once every 90 min. Therefore, two beamlines, referred to as the 'Backlighter' and 'Sidelighter', were alternately used to double the number of experimental shots. For this experiment, spatially filtered apodizers were inserted before the final focusing off-axis parabolic mirror to control the beam diameter and improve the focal spot characteristics of each beamline [37]. The f/6 apodizer configuration increased the Rayleigh length by a factor of approximately 10 relative to the native f/2 final focusing optic. With this setup, the apodized beams produced focal spots with a nominal beam waist, $w_0$ which ranged from $13.5 - 17.3\,\mu$m, and delivered up to 85 J (49 J) of laser energy on the Backlighter (Sidelighter) beamlines; this configuration resulted in nominal peak normalized vector potentials of $a_0 = 5.4$ ($a_0 = 4.4$), corresponding to nominal peak laser intensities of $3.61 \times 10^{19}\,\mathrm{W\,cm}^{-2}$ ($2.46 \times 10^{19}\,\mathrm{W\,cm}^{-2}$).

For certain experimental laser shots, (as identified in later figures) an ICS foil was placed after the gas jet at a 15° angle with respect to the electron beam axis, where it generated a highly reflective surface

plasma. Since the electron and the pump laser both travel at approximately the speed of light, most of the electrons collide with the reflected laser photons despite the small angle. The use of a low-$Z$ ICS foil may raise the concern that the laser's pre-pulse could ablate the foil well before the arrival of the main pulse, thereby skewing the results and suppressing the ICS mechanism. However, the incoherent focal spot of the EP pre-pulse reaches a peak intensity of only $\sim 1.6 \times 10^{12}\,\mathrm{W\,cm^{-2}}$ about 1.2 ns before the main pulse, compared to a main-pulse peak intensity of $5.9 \times 10^{19}\,\mathrm{W\,cm^{-2}}$, corresponding to an intensity contrast of ~76 dB [38]. Consequently, any pre-pulse interaction with the foil is negligible, and the ICS foil is expected to remain intact during the main pulse, ensuring that the ICS mechanism is not compromised by unintended properties of the OMEGA EP laser system.

The diagnostic assembly was positioned 47.63 cm downstream of the gas jet. A nominal 0.8 T magnetic field, generated by a 10.48 cm dipole magnet, dispersed the electron beam after it passed through a 5 mm × 5 mm square aperture in the electron spectrometer, inset 6.88 cm from the front surface of the diagnostic. The combined electron–proton spectrometer employed a cylindrical outlet aperture 8 mm in diameter and 13.8 mm in length to terminate charged particles before they reached the photon diagnostic.

The x-ray diagnostic system arranged metal filters in a spoke-wheel geometry (filter wheel), followed by stacked metal layers interleaved with image plates (IPs), and inset this assembly 109.92 cm from the front surface of the diagnostic. Shaw *et al* [34] provides further details on beam charge, divergence, source size, and pointing stability.

We varied the gas pressure (plasma density) and laser energy, while also repeating experimental shots to quantify both the reliability of the platform and the variability of the electron beam and x-ray source for a given set of input parameters.

### 2.1. Results & discussion

#### *2.1.1. Electron spectrum*

In experiments described here, the laser-plasma produced relativistic electron beams were detected 54.5 cm downstream, where they were measured using an electron positron proton spectrometer (EPPS) mounted on a 10 inch manipulator and equipped with a blast shield [34, 39] (figure 2). The spectrometer housed a stack of IPs positioned perpendicular to the beam axis to capture information about the beam's transverse distribution, angular spread, pointing stability, and charge. The front stack included a 25 $\mu$m thick aluminum filter to eliminate residual laser light, followed by two BAS-MS IPs. The first plate served as an energy filter, suppressing electrons below approximately 400 keV, while the second plate captured the spatial and charge distribution of higher-energy electrons that penetrated the filter. In the experiment, the front plates had a central 5 mm aperture, enabling on-axis high-energy electrons to pass through to the EPPS spectrometer. The EPPS has a high-energy, low-dispersion 0.8 Tesla magnet configuration, which bends the propagating electrons onto an IP oriented facing orthogonal to the axis of propagation. This electron spectrometer is capable of resolving energies up to 200 ± 20 MeV [34, 39].

A dedicated analysis suite was used to process the raw IP data and extract the electron spectra. The Fujifilm BAS-IP SR IPs were scanned using a Fujifilm Typhoon FLA7000 imager system with a spatial resolution of $100 \times 100\,\mu\mathrm{m}^2$, dynamic range of L5, laser voltage sensitivity setting of S4000, and a photomultiplier voltage of 687 V. The resulting proprietary 16 bit .gel files were converted into photostimulated luminescence (PSL) units using these parameters as described by equation 1 of Williams *et al* Rev. of Sci. Inst. 2014 [40–42]. The central portion of the electron beam-illuminated diagnostic images were then vertically averaged and converted into a lineout to represent the energy-resolved signal across the dispersion axis. A narrow background region, taken from the top two pixels of each plate, was subtracted from the signal to isolate beam-induced luminescence from the background electron signal of secondary electrons and light emission. The horizontal pixel coordinates were mapped to electron energy using a pre-characterized EPPS dispersion curve as per Shaw *et al* [34]. Signal decay due to the time elapsed between experimental shot and IP scan was corrected using a double-exponential fading model, equation 3 of Maddox [43], and absolute electron yield was calculated by applying an energy-dependent PSL-to-charge conversion. The resulting electron spectrum was fit with a two-component exponential function, $f(E) = A_1 \mathrm{e}^{-\frac{E}{T_1}} + A_2 \mathrm{e}^{-\frac{E}{T_2}}$ using a base-10 logarithmic transform of the dependent variable. Fitting in log space improves numerical stability by compressing the dynamic range of the data (which spans two to three orders of magnitude between 1 and 200 MeV), thereby reducing the number of function evaluations required to reach the target coefficient of determination ($R^2$). In this form, the trust region reflective algorithm solves a problem that is closer to linear in the transformed space, leading to faster convergence compared to a direct fit in linear space [44, 45]. From this fit, the amplitudes and characteristic energies ($A_1$, $T_1$, $A_2$, $T_2$) were extracted, and 95% confidence intervals were estimated from the parameter covariance matrix [44].

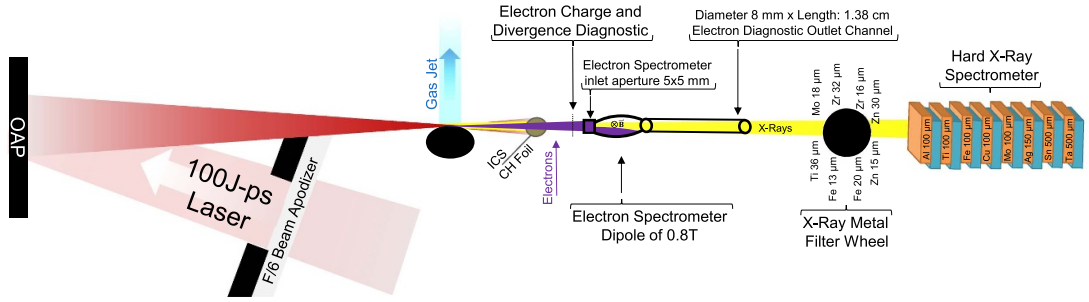


**Figure 2.** Schematic layout of the experimental platform. The two lasers beams are orthogonally oriented with the 'Backlighter' beam delivering a maximum $f/6$ energy of 85 J and the 'Sidelighter' beam providing a maximum $f/6$ energy of 45 J. These beams share a gas jet (6/8 mm dia.) at the chamber centered and duplicate, identical diagnostics are fielded for each laser beam.

The $A_1$ and $T_1$ parameters are representative of the population of SMI accelerated electrons, as determined by PIC simulations, which are the dominant source of accelerated electrons in the 1–40 MeV range [46]. In contrast, the $A_2$ and $T_2$ parameters of the two-temperature exponential fit represent electrons accelerated via other mechanisms such as DLA, which dominates above 60 MeV [46]. We note that DLA occurs in both the plasma channel that forms right behind the self-modulated plasma wave due to relativistic self-focusing, and by overlap of the electrons accelerated by the longitudinal field with the transverse field of the laser in the presence of ions [47].

It is important to note that placing an ICS foil should have very little effect on the electron spectra [9]. The plasma produced by the picosecond laser pulse on the surface of the foil can affect the emittance (and hence the divergence angle) of the low energy electrons ($E \lesssim 10$ MeV), but should not affect either the yield or temperature of the high energy electron beam. The two-temperature fit represents the sum of the SMI and DLA effects, which produce two quasi-Maxwellian populations. As might be expected, the electron spectra from gas-jet-alone shots (betatron with DLA) were tightly grouped, with $T_1$ temperatures in the 18 MeV range for SMI-accelerated electrons and 50–60 MeV temperatures for the $T_2$ fit component attributed to DLA-accelerated electrons, (figures 3(b) and (c)). In our mathematical model of these gas-jet-alone shots, the smaller $T_1$ value reflects a 'cold' electron population, characteristic of the substantial charge accelerated in the multitude of EPWs driven by the SMI, whereas the larger $T_2$ value corresponds to a 'hot' population originating from DLA, for the respective energy ranges as described by [46]. In comparison to the gas-jet-alone shots, the experimental shots with ICS converter foils driven with comparable lasers $a_0$ (4.5–5.4) had more substantial spread in electron spectra (purple data points). We attribute the spread of fit parameters associated with ICS shots to the shot-to-shot variation of the gas plume profile, number of e-foldings of the SMI, stochastic variations of the DLA, and absolute pointing stability of the accelerator. For the lower count of gas-jet-alone shots, by happenstance, all exhibited similar electron beam spectra (figures 3(b) and (c)) even though the accelerated electron beam was subject to the same variability. Specifically, two ICS shots (facility shot number #38 391 & #38 396) exhibited elevated electron $T_2$ temperatures, ~70 MeV, but these higher $T_2$ temperatures were correlated with reduced electron yield 1.59e+12 Particles/sr/MeV and 9.02e+11 Particles/sr/MeV. The two ICS-coupled shots with low $T_1$ temperatures (data points at 11 and 15 MeV, facility shot numbers #38 400 figure 3(a), & #38 404), held the highest yield at 1.03e+13 Particles/sr/MeV and 9.81e+12 Particles/sr/MeV at temperatures of 46.8 MeV & 46.2 MeV, respectively. These ICS shots outperformed the gas-jet-alone configuration experimental shots, which all were grouped around 50–60 MeV. Importantly, when averaged over all high-energy (>80 J) shots, the gas-jet-alone and ICS configurations produced comparable mean beam charge, 0.9 $\mu$C sr$^{-}$1, while being characterized by some variance in the fitting parameters as described by the per shot discussion above. By contrast, the lower-energy (<80 J) subsets for both configurations showed greater variability in all fit parameters, reflecting the increased sensitivity of SMI growth, DLA onset, and beam loading to drive energy and instantaneous plasma conditions at reduced normalized laser intensity, $a_0$.

In summary, the SMI and DLA mechanisms produced remarkably consistent results across multiple shots ranging from $a_0$ of 4.5 to 5.4 (> 80 J). Somewhat surprisingly, the electron spectra on the experimental shots with ICS foils showed broader electron spectra. The origin of this effect is not yet understood, as neither the total yield nor the temperature of the accelerated electrons was expected to be significantly altered by the low-$Z$ plasma generated on the surface of the ICS foil by the residual drive laser pulse.

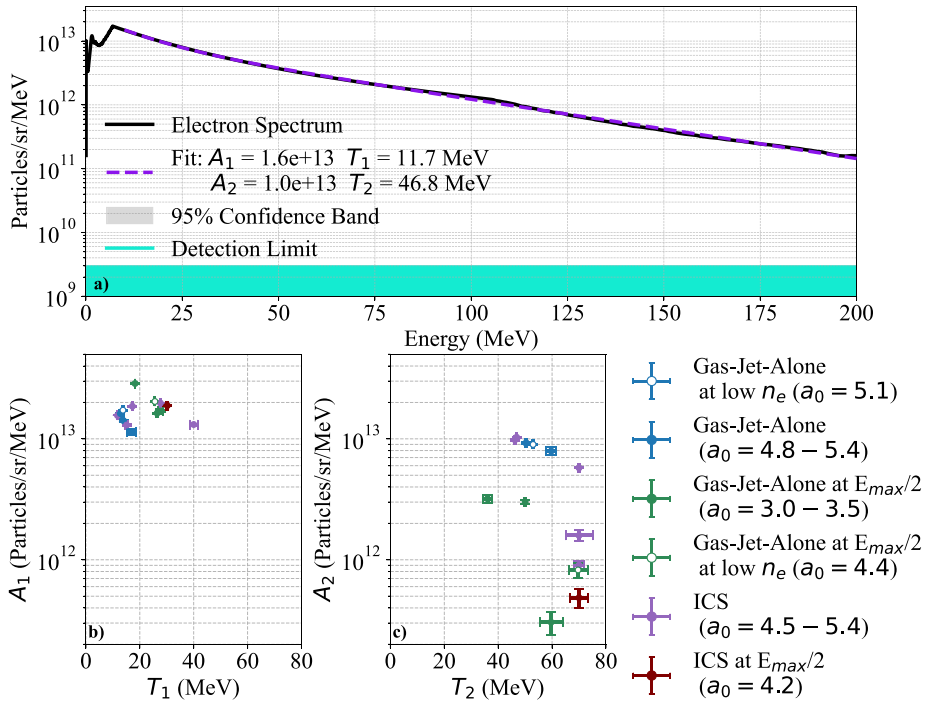


**Figure 3.** Example electron spectra (a) of an electron beam generated by the underdense plasma interactions. The example spectrum is for the experimental configuration where the electrons transferred energy to the reflected laser photons by propagating through a low-$Z$ ICS foil. This and other laser-produced electron beams (b), (c) were fit to a two exponential fit $A_1 e^{-E/T_1} + A_2 * e^{-E/T_2}$ to quantify temperature and yield of the electron spectra.

*2.1.2. X-ray analysis method*

After passing through the filter wheel the x-rays expose a stack of IPs, separated by variable-thickness metal foils that act as an x-ray spectrometer. An example of the exposure produced on the first IP is shown in figure 4(a) with recovered spectrum shown in figure 4(b). In figure 4(b), (as well as the following figure) the $y$-axis denotes the photon yield, expressed as $\gamma$/keV/sr, corresponding to the number of photons emitted per unit photon energy and per unit solid angle.

The IPs used for x-ray detection were also scanned using a Fujifilm FLA-7000 650 nm laser scanner. The BAS-SR IPs were scanned with a spatial resolution of $100 \times 100\ \mu m^2$ while the x-ray IP stack was scanned with a laser sensitivity setting of S1000, photomultiplier tube voltage of 687 V, and with a dynamic range of Latitude 5. The scanned IPs were converted from raw 16 bit intensity counts to PSL using a calibration procedure based on the aforementioned scanner resolution, sensitivity, and a standard response model for photons [42]. For each metal filter region on the filter wheel, a circular region of approximately $r = 300\ \mu m$, centered around the diagnostic's 5 mm aperture, was averaged to obtain a transmitted intensity. The mean PSL value within that region was used to represent the transmitted signal, and the standard deviation of pixel values was used to estimate the uncertainty due to spatial variation of the PSL counts associated with the transmission through these metal filters.

The filter wheel contained the following metal foils, identified clockwise from the 12 o'clock position: Zr (16 $\mu$m), Zn (30 $\mu$m), Zn (15 $\mu$m), Fe (20 $\mu$m), Fe (13 $\mu$m), Ti (36 $\mu$m), Mo (18 $\mu$m), and Zn (32 $\mu$m), see figure 4(a). These foils were selected to form both Ross and differential attenuation thickness (DAT) pairs. Ross filter pairs-constructed from different elements with nearby $K$-edges-include Zn 15 $\mu$m/Fe 20 $\mu$m (7.1–9.6 keV), Zr 16 $\mu$m / Zn 30 $\mu$m (9.6–18.0 keV), and Mo 18 $\mu$m / Zr 32 $\mu$m (18.0–20.0 keV). For Ross pairs, the spectral datapoint is defined as follows: the center point is the mean photon energy of the $K$-edge window; the horizontal error bars correspond to the bandwidth of this bandpass filter, the difference between the two material's $K$-edges; and the vertical error bars represent the transmission fraction above or below the window, respectively. In the ideal case, the transmission difference outside the $K$-edge window vanishes, describing a theoretically perfect bandpass filter. DAT filter pairs comprising the same element but different thicknesses include Zr (16/32 $\mu$m), Zn (15/30 $\mu$m), and Fe (13/20 $\mu$m). For DAT filter pairs, the center point is now defined as the transmission-weighted mean photon energy, with the horizontal error bar now corresponding to the bandwidth between the 25% and 75% percentiles of the cumulative transmitted photon fluence. The vertical error bars are defined analogously to Ross filter pairs, with the positive error bar corresponding to the transmission

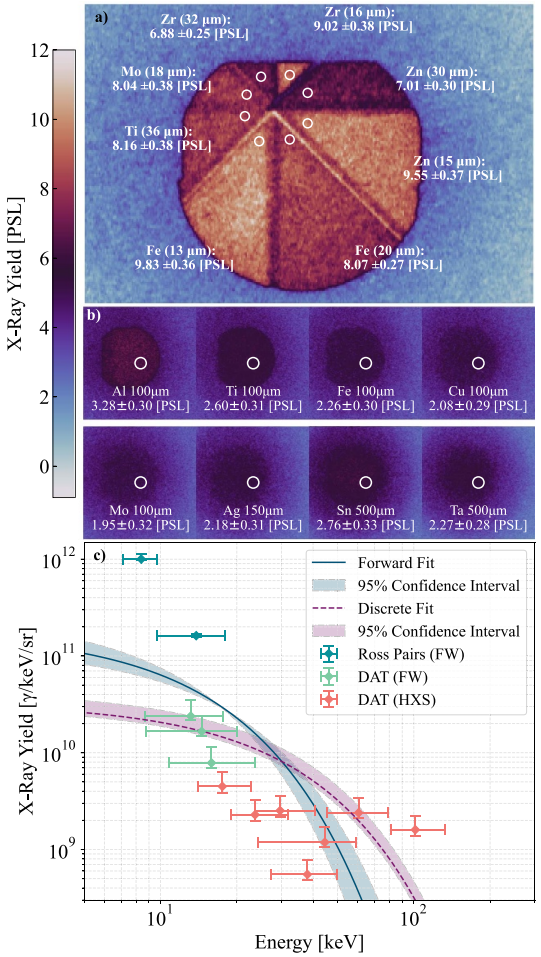


**Figure 4.** Example x-rays detected on the diagnostics image plates via the filer wheel (a) & stacked metal spectrometer (b). Panel (c) contains the resulting analysis from the Ross (Blue) and DAT (Teal) pairs of the filter wheel, the DAT (Orange) pairs of the stacked metal spectrometer along with theoretically fitted curves. See the text for details.

above this window and the negative error bar corresponding to the transmission below this transmission weighted window. The PSL fluences for all filters are shown in figure 4(a), and the resultant spectral data points inferred from the Ross and DAT pairs are plotted in figure 4(b).

Of the three possible Ross pairs, only two provided useful data, as the Mo 18 $\mu$m / Zr 32 $\mu$m (18.0–19.9 keV) *K*-edge window resulted in anomalously high spectral fluence, likely due the observed transmission, PSL, through the two foils being too similar to each other, in comparison to the other Ross Pairs. This is likely due to the signal-to-noise ratio of the illumination across the IP and/or the detected x-ray spectrum being unduly influenced from background x-ray generation of the electron beam striking the containment walls of the EPPS detector.

In addition to the filter wheel we employed a reduced-channel hard x-ray spectrometer (HXS) based on the diagnostic design of Chen *et al* [48]. This instrument consists of a linear stack of nine high-*Z* filters. By sampling the transmitted fluence through increasing atomic number and thickness, this spectrometer provides sensitivity to the 15 keV — 132 keV hard x-ray band and enables sequentially ordered DAT pairs for spectral extraction. These HXS DAT pairs are: Ti 100 $\mu$m & Al 100 $\mu$m (15–24 keV), Fe 100 $\mu$m & Ti 100 $\mu$m (20–33 keV), Cu 100 $\mu$m & Fe 100 $\mu$m (24–42 keV), Mo 100 $\mu$m & Cu 100 $\mu$m (28–50 keV), Ag 150 $\mu$m & Mo 100 $\mu$m (25–60 keV), Sn 500 $\mu$m & Ag 150 $\mu$m (46–80 keV), and Ta 500 $\mu$m & Sn 500 $\mu$m (81–132 keV). These hard x-ray DAT pairs provide transmission-weighted midpoints spanning 18.8–102 keV, with corresponding 25%–75% bandwidths ranging from 9.2 keV in the lowest-energy pair to 51 keV in the highest-energy pair. The sequential DAT configuration of the HXS substantially expands the number of available spectral constraints-from five Ross and DAT pairs on the filter wheel alone to twelve when the stacked-metal spectrometer channels are included-thereby providing additional empirical leverage on both the spectral slope and high-energy tail of the analytical models used in the curve fitting analyses.

To reconstruct the incident x-ray spectrum, both forward-fitting and discrete analysis methods were employed [49].The discrete fitting method employs a weighted nonlinear least-squares routine [50] to fit the analytical functions $f(E;A_c,E_c)$ or $f(E;A_1,E_1)$ to the Ross and DAT pair data. To mitigate the influence of the high-yield Ross pairs, the fit was performed in $\log_{10}$ space, thereby weighting the analytical function in a manner that emphasizes the lower-yield DAT pairs. The forward fit method is an inversion routine that estimate the energy spectrum of x-rays by comparing measured IP responses behind various metal filters to predictions from an analytical model. Instead of directly trying to 'unfold' the spectrum from measurements (which can be unstable or ambiguous), this method starts with an analytical model of the expected functional form of the x-ray spectrum. This analytical model is used to calculate how much signal each filter should produce by accounting for how each material absorbs x-rays at different energies and how sensitive the IPs are to those energies. In this implementation, the forward-fit method computes synthetic PSL values for each of the eight metal filters using

$$P_{\mathrm{calc},i} = \int T_i(E)\, R(E)\, f(E;E_c,A_c)\, dE,$$

where $T_i(E)$ is the energy-dependent transmission of the $i$th metal filter (including all upstream materials), $R(E)$ is the calibrated energy response of the IP, and $f(E;A_c,E_c)$ or $f(E;A_1,E_1)$ is the assumed spectral model (synchrotron-like for gas-jet-alone shots or exponential for ICS shots) parameterized by amplitude ($A_c$, $A_1$) and characteristic energy ($E_c$, $E_1$). The resulting vector $P_{\mathrm{calc},i}$ is supplied to a weighted nonlinear least-squares routine [50], which adjusts the input parameters ($E_c$,$A_c$ or $E_1$,$A_1$) so that these analytically generated PSL predictions best match the experimentally measured values $P_{\mathrm{meas},i}$ for each filter channel, thereby providing a physically constrained inversion of the x-ray spectrum [49, 51, 52].

For the shots with experimental configurations that only generated hard x-rays from the betatron radiation emitted from the underdense plasma (gas-jet-alone) we can utilize $\frac{\mathrm{d}^2I}{\mathrm{d}E\mathrm{d}\Omega} = A_c \times 10^{10}\frac{1}{E}\left(\frac{E}{E_c}\right)^2 K_{2/3}^2\left(\frac{E}{E_c}\right)$, where $E$ is the energy of the emitted x-rays, $E_c \propto \gamma^2 n_e r_b$ is the critical energy, and $K_{2/3}$ is the modified Bessel function of the second kind [32]. This equation models the on-axis observation of the resultant betatron x-ray spectra. For the experimental laser shots with both the underdense plasma and the low-$Z$ ICS foil, we employed an exponential fit, $f(E;E_1,A_1) = A_1 \times 10^{10}\mathrm{e}^{-E/E_1}$, where now $A_1$ is the amplitude of the decaying x-ray spectrum and $E_1$ is the effective spectral temperature (i.e. the fitting parameter), which represents the characteristic energy scale over which the spectrum decreases by one e-folding. The expected PSL values for each filter are computed by convolving the assumed spectrum with the filter transmission and IP response functions, and then iteratively adjusting to minimize residuals with the measured PSL. In parallel, discrete analysis was performed using Ross and DAT pairs, as described above [49]. Together, these methods provide a robust, multi-pronged analysis of the x-ray spectrum across a broad energy range, ensuring internal consistency and resilience to filter-specific artifacts (i.e. non-uniform x-ray transmission across a metal foil).

*2.1.3. X-ray comparison between gas-jet-alone spectrum and gas-jet with inverse compton scattering*

A key distinction between the various spectral analysis methods used in this work lies in their treatment of spectral shape and resolution. The Ross and DAT pairs figure 5(a), evaluate x-ray transmission through specific filter combinations to determine the relative fluence across well-defined energy bands (e.g. 7–18 keV). This technique is robust in determining the transmission over the filter windows, however, it lacks the capacity to reconstruct continuous spectral structure (whereas forward fitting can), making it less suited for characterizing broad or high-energy tails.

From a base-10 discrete fit to the Ross and DAT filter pairs, ICS-enhanced shots yielded an average amplitude of $A_1 = (2.96 \pm 0.41)$ Ph keV sr$^{-1}$ and a characteristic energy of $E_1 = 19.6 \pm 6.03$ keV across $N = 5$ shots, figures 5(d) and (e). A single low energy ICS shot, figure 5(f), yielded $A_1 = 0.62$ Ph keV sr$^{-1}$ with characteristic energy of $E_1 = 50$ keV (limited to the upper bound of the least squared fit). Across the gas-jet-alone configurations, the discrete fit analysis characterized parameter scaling. High-energy shots 5(a) produced $A_c = 1.67 \pm 0.90$ Ph keV sr$^{-1}$ and $E = 31.10 \pm 5.74$ keV for $N = 3$ shots. Lower-energy shots 5(b) exhibited reduced amplitude, $A_c = 0.636 \pm 0.518$ Ph keV sr$^{-1}$, but substantially higher effective spectral temperatures, $E_c = 82.58 \pm 101.68$ keV, again for $N = 3$ shots. Finally, in the low-density regime 5(c), a single shot yielded $A = 1.028$ Ph keV sr$^{-1}$ and $E = 25.17$ keV. These characteristic x-ray spectra indicate that ICS-enhanced spectra, while lower in x-ray temperature $E_1$, typically outperform gas-jet-alone spectra in the diagnostic range by a factor of greater than 10×, according to discrete analysis. Although the ICS electron spectra (figure 3) exhibit significant variance in the temperatures and amplitude of the recovered electron spectrum, the associated x-ray output remains remarkably consistent in both amplitude and energy, confirming the robustness and reproducibility of ICS-generated radiation.

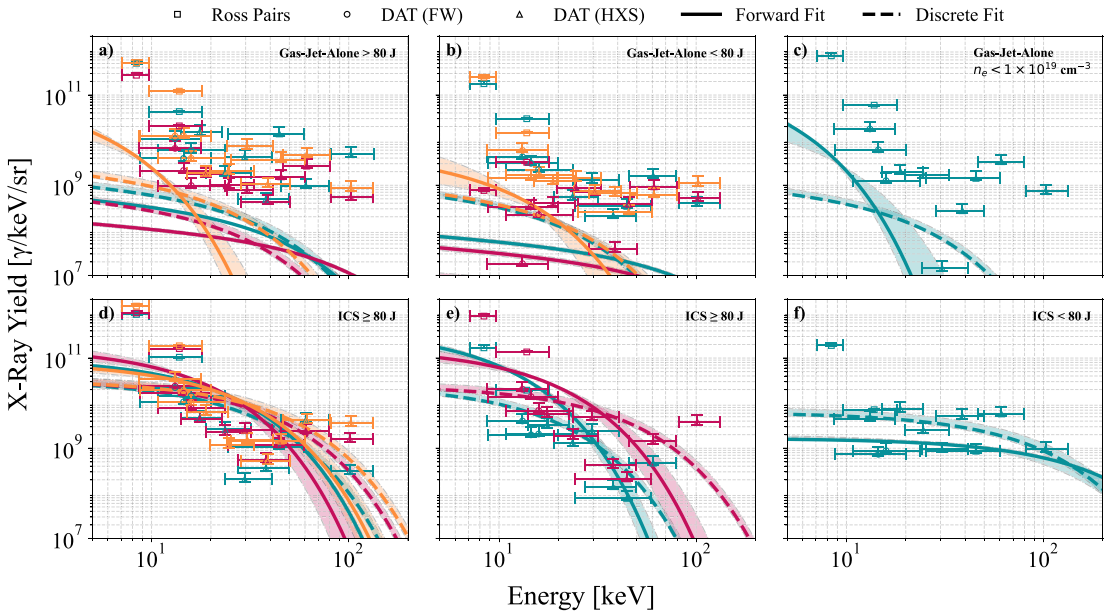


**Figure 5.** Examples of x-ray spectra (a)–(c) described by forward fitting, discrete fitting and the Ross filter pairs & DAT filter pairs as produced by the x-rays emitted by betatron radiation from the electrons in the underdense plasma in gas-jet-alone configuration. Panel (a) is for laser parameters above 80 J, panel (b) less than 80 J, and panel (c) is when plasma density was below $1\times10^{19}$ cm$^{-3}$. Panel (d)–(e) are for shots with laser energy above 80 J with both betatron radiation and ICS from employing a low-$z$ (CH-plastic) foil (shot collection split only for illustrative purposes). Panel (f) is for the same prior configuration, but for laser energy of 49 J.

In contrast to the Ross and DAT filter pairs discrete fit analysis method, the forward-fit technique (figure 5(c)) applies a parametric model-typically synchrotron-like or exponential-to the full set of filter-resolved PSL data. Using least-squares optimization, it incorporates both filter attenuation and detector response to reconstruct a continuous spectrum and enable statistical comparisons across shots. However, because the forward fit emphasizes global spectral structure, particularly at higher energies, it often underestimates the photon fluence in the lower-energy range. This discrepancy arises from its reduced sensitivity to localized spectral contributions that are more directly captured by the discrete method (e.g. through transmission windows of the Ross filter pairs). As a result, the forward fit tends to underpredict these lower intensity photon yields.

Forward-fit analysis of the filter-wheel PSL data revealed clear spectral trends that arise from variations in the scanned laser energy, plasma density, and the presence or absence of the ICS foil. The gas-jet-alone shots are grouped by three experimental parameter regimes. High-energy betatron shots, figure 5(a), produced an average amplitude of $A_1 = 9.55 \pm 15.27$ Ph keV sr$^{-1}$ and a characteristic energy of $E_1 = 51.0 \pm 47.3$ keV ($N = 3$). Lower-energy betatron shots, figure 5(b), generated a smaller amplitude, $A_1 = 1.06 \pm 1.51$ Ph keV sr$^{-1}$, but a significantly harder spectral falloff with $E_1 = 70.8 \pm 50.6$ keV ($N = 3$). The single low-density betatron shot, figure 5(c), produced a distinctly different response, with a large amplitude $A_1 = 57.2$ Ph keV sr$^{-1}$ and a soft energy scale $E_1 = 4.27$ keV, which is consistent with a larger plasma volume, but lower number of accelerated electrons, hence the lower x-ray temperature. Comparing the forward fits of the gas-jet-alone to the ICS foil shots, we identify two ICS experimental parameter regimes. The low-energy ICS shot, figure 5(f), produced a small amplitude of $A_1 = 0.166$ Ph keV sr$^{-1}$ but a very hard spectrum with $E_1 = 100$ keV (limited to the upper bound of the least squared forward fit), indicating efficient high-energy photon generation despite reduced low energy x-ray fluence. In contrast, the collection of high-energy ICS shots, figure 5(d) & e, yielded markedly enhanced forward-fit parameters, with $A_1 = 19.24 \pm 14.09$ Ph keV sr$^{-1}$ and $E_1 = 10.37 \pm 3.38$ keV across $N = 5$ shots. These results demonstrate that ICS consistently enhances the photon yield while producing a softer exponential spectral slope, whereas betatron-dominated spectra show substantially greater shot-to-shot variability as the x-ray generation is solely dependent upon the evolution of gas-jet plasma dynamics (SMI and DLA).

Looking forward, the directional hard x-ray source is well positioned for integration with bremsstrahlung converters, which can substantially extend the x-ray spectrum into the MeV regime [27], albeit with reduced photon flux over the 1 keV to as high as the 100 keV photon range. Together, the discrete and forward-fit analyses demonstrate a complementary picture of betatron and ICS emission: betatron radiation offers broadband, high-fluence output ideal for a wide range of imaging, and ICS acts

**Table 1.** Comparison of the parameters used for the (a) laser, (b) focal system, and (c) plasma, as well as the results obtained for the (d) electron and (e) x-ray spectra on two sister facilities, the Titan Laser System at JLF and OMEGA EP Backlighter/Sidelighter Laser System at LLE.

| | System parameters | | | | |
|---|---|---|---|---|---|
| | Laser | Wavelength | Pulse duration | Energy | Peak $a_0$ |
| JLF | Titan | 1053 nm | 700–1000 fs | 80–150 J | 3 |
| EP | EP Back/Sidelighter | 1053 nm | 700 ± 100 fs | 45–84 J | 5.4 |
| | Focal system | | | | |
| | Type | f/# | Spot size | | |
| JLF | OAP | $f/10$ | 29 $\mu$m | | |
| EP | Apodizer | $f/6$ | 12 $\mu$m | | |
| | Plasma target | | | | |
| | Type | Diameter | Gas | Density $\times 10^{18}$ cm$^{-3}$ | |
| JLF | Supersonic nozzle | 3, 4, 10 mm | He,He/He:N2,He | 5–15, 1–5, 1–10 | |
| EP | Mach 6 nozzle | 6, 10 mm | He | 7–17 | |
| | Electron spectrum | | | | |
| | $T_1$ (MeV) | $T_2$ (MeV) | $A_1 \times 10^{12}$ (e$^-$/MeV/sr) | $A_2 \times 10^{12}$([e$^-$/MeV/sr) | |
| JLF | 7–18 | 20–50 | 1.08E-01[a] | 1.80E-03[a] | |
| EP | 11.7–40 | 36–70 | 11–28 | 0.3–10 | |
| | X-ray spectrum models | | | | |
| | $A_c$x10$^{10}$ (Ph keV Sr$^{-1}$) | $E_c$ (keV) | $A_1$x10$^{10}$ (Ph keV Sr$^{-1}$) | $E_1$ (keV) | |
| JLF | 6–36 | 8.5–19.7 | 1.2–5.6[b] / 0.89–1.75[c] | 8.7–13[b] / 23.9–29.0[c] | |
| EP | 0.4–57 | 4–100 | 8.3–43 | 5.3–14.1 | |

[a] Normalized against $\Omega_{det} = 0.01$ sr.
[b] Diagnostic band from Filter Wheel [49].
[c] Diagnostic band from Hard x-ray Spectrometer 'Cannon' [49].

as a booster to the betatron emission in both yield and x-ray energy range to strengthen the applicability of this directional hard x-ray source for HEDS experiments.

*2.1.4. High level comparison between JLF Titan results and OMEGA EP Backlighter/Sidelighter results*

The Titan Laser at JLF (80–150 J, 700–1000 fs, $a_0 \sim 3$) and the OMEGA EP Back/Sidelighter system (45–85 J, 700 fs, $a_0 \sim 5.4$) were each focused with $f/10$ or $f/6$ optics to 29–12 $\mu$m spots into Mach 3–5 or Mach 6 gas jets with densities ranging from 1–17 $\times$ 10$^{18}$ cm$^{-3}$, as detailed in table 1. These configurations produced electron spectra with temperatures up to 50–70 MeV and x-ray emission characterized by Betatron-like spectra extending from ∼10 keV up to ∼300 keV. The measured source size is ∼100 $\mu$m FWHM [25], consistent with point-projection imaging requirements.

The characteristic electron spectra driven by the Titan laser exhibited $T_1 \sim 7$–18 MeV and $T_2 \sim 20$–50 MeV, whereas the OMEGA-EP laser produced hotter distributions of $T_1 \sim 11.7$–40 MeV and $T_2 \sim$ 36–70 MeV, indicating a flatter spectrum that extended further into the high-energy electron range, as per table 1. This behavior is reflected in the betatron x-ray output: Titan shots yielded $A_c \sim 6$–36$\times$10$^{10}$ ph keV sr$^{-1}$ with critical energies $E_c \sim 8.5$–19.7 keV, while the forward-fit values obtained on OMEGA-EP spanned a wider range of $A_c = 0.4$–57$\times$10$^{10}$ ph keV sr$^{-1}$ and $E_c = 4$–100 keV. The larger $E_c$ values observed on OMEGA-EP, particularly in lower-energy ($a_0$) shots, correspond to significantly harder spectra but with reduced fluence in the 1–10 keV band relative to Titan. A similar trend appears in the ICS results: Titan produced $A_1 \sim 1.2$–5.6 (0.89–1.75 in the Cannon spectral range)$\times$10$^{10}$ ph keV sr$^{-1}$ at $E_1 \sim 8.7$–13 keV (23.9–29.0 keV in Cannon), whereas OMEGA-EP ICS shots exhibited a broader range of $A_1 = 8.3$–43.3 $\times$ 10$^{10}$ ph keV sr$^{-1}$ and $E_1 = 5.3$–14.1 keV, as listed in table 1. Thus, while both facilities demonstrated broadly comparable hard x-ray sources driven by picosecond lasers, OMEGA-EP achieved these spectral results with less than 85 J on target, whereas Titan required up to 65 J more energy to produce qualitatively similar spectra. This enhanced efficiency at OMEGA-EP arises from the use of a spatial apodizer to replicate a shorter f-number optic, which reduces the focal spot size and thereby increases $a_0$, compensating for the lower delivered energy relative to Titan.

This compact, directional hard x-ray source thus bridges the ∼10 keV band (critical for phase-contrast and low-$Z$ interface imaging) with >50 keV capability using ICS-enabling penetration of dense targets. Placing a high-$Z$ converter foil can further increase the photon energy into the MeV range by incorporating electron beam-bremsstrahlung radiation. Such brightness and tunability are critical for OMEGA and OMEGA-EP campaigns that demand directional radiography rather than those based on point projection imaging [53, 54]. Experiments that would benefit from such a radiographic source include early-time hydrodynamics [28], growth of seeded hydrodynamic instability [29], the break-up and mixing of low-$Z$ interfaces [30], dense directly-driven implosions [31], coil-laden MIFEDS targets [55], thick metal shock tubes [7], and areal density ($\rho R$) measurements of deuterium–tritium filled spherical capsule implosions [2, 56].

The applicability of this source extends broadly to shock-imaging experiments. Ultrafast betatron radiography of laser-driven shocks in silicon by Wood *et al* [57] highlights the potential of compact x-ray sources for probing solid-density dynamics. Unlike traditional surface-based diagnostics such as high-speed photography or velocity interferometry [58], which are restricted to measuring shock breakout and surface velocities, directional hard x-rays can directly probe subsurface structures and thereby capture the temporal and spatial evolution of laser-driven shocks. tabletop single-shot phase imaging of shocked targets [59] has already demonstrated phase-sensitive contrast and recently, the x-ray phase-contrast imaging method discussed in this work has been utilized at OMEGA EP using laser-driven Cu–(CH) foil backlighters [30]. For all these experiments the directional hard x-ray source proposed here would be advantageous compared to such low-$Z$ foil bremsstrahlung sources, as it provides true point-projection imaging with tunable photon energy and significantly higher flux. Similarly, point-projection radiography of buried-cone targets at LULI [60] would benefit from the increased brightness and >50 keV capability needed to penetrate cone walls and resolve shock propagation in dense assemblies. Proton radiography of shock-compressed carbon foams [61] could also be complemented by broadband hard x-ray imaging, which enables attenuation-based density mapping with higher spatial resolution and provides a direct comparison to charged-particle diagnostics.

## 3. Summary

Before a new diagnostic for HEDS experiments is adopted on a major laser facility, such as National Ignition Facility, it has to be tested for reliability and robustness on at least two laser facilities with similar power. Our experimental platform uses picosecond laser pulses interacting with an underdense plasma to generate and accelerate relativistic electrons that emit betatron x-rays within the plasma, augmented by ICS radiation. This paper reports our results obtained on the OMEGA EP laser facility at LLE. The results are in good agreement with our previous results obtained using the Titan Laser at the Jupiter Laser Facility at LLNL, where x-ray fluences were recorded to be $6-36$ $(1.2-5.6^{a}, 0.89-1.75^{b})$ $\times 10^{10}$ Ph keV Sr$^{-1}$ at $8.5-19.7$ $(8.7-13^{a}, 23.9-29.0^{b})$ keV for Betatron (ICS) generated photons. Two spectral analysis techniques-discrete filter-based fitting and forward model fitting-were employed to extract spectral amplitudes and critical energies across a range of experimental conditions. While the forward fit resolves full spectral profiles, it systematically underestimates fluence within the 7–18 keV band compared to the more robust, window-specific Ross Pair and Differential Averaged Transmission filter technique. Betatron sources produced broadband emission with minimal shot-to-shot variability, whereas ICS-enhanced shots occurred with more variable, but exhibited higher electron energy, x-ray energy, and fluence, with average x-ray yields exceeding betatron emission by up to an order of magnitude. These results highlight the complementary strengths of betatron and ICS emission and establish that this directional hard x-ray source driven by a sub-picosecond, 100-TW-class laser is a viable and flexible source for HEDS experimental diagnostics.

## Acknowledgments

Thanks to OMEGA EP operation teams, we had multiple successful shot days and collected datasets large enough to evaluate statistics of this platform's performance. This work was supported by the following agencies and grants, Department of Energy (DOE) Grant No. DE-SC0010064:0011, Lawrence Livermore National Laboratory (LLNL) B669933, and the University of California, Los Angeles. This material is based upon work supported by the Office of Fusion Energy Sciences under Award Numbers DE-SC0021057 and the Department of Energy (DOE) [National Nuclear Security Administration (NNSA)] University of Rochester 'National ICF Program' under Award Number DE-NA0004144.

This report was prepared as an account of work sponsored by an agency of the U S Government. Neither the U S Government nor any agency thereof, nor any of their employees, makes any warranty,

## Data availability statement

The data cannot be made publicly available upon publication because they are owned by a third party and the terms of use prevent public distribution. The data that support the findings of this study are available upon reasonable request from the authors.

## Author contributions

The experiments were performed by M. S., N. L., J. S., I. P., A. A., P. K., C. A. and F. A. Experimental data was processed and analyzed by M.S. as well as I.P., A.A., and P.K. Simulations and theory were supported by N. L., K. M., and F. A. The manuscript was primarily written by M.S. and C.J.

## ORCID iDs

Mitchell Sinclair 0000-0002-2723-4881
Isabella Pagano 0000-0001-6103-2389
Nuno Lemos 0000-0002-6781-5672
Charles D Arrowsmith 0000-0001-6186-2227
Jessica L Shaw 0000-0002-1118-8921
Kyle G Miller 0000-0003-4826-9001
Paul M King 0000-0003-3424-6386
Adeola Aghedo 0000-0001-9909-2213
Kenneth A Marsh 0000-0002-2929-3682
Gianluca Gregori 0000-0002-4153-0628
Félicie Albert 0000-0002-4612-8240
Chan Joshi 0000-0002-1696-9751

## References

[1] Remington B A *et al* 2019 *Proc. Natl Acad. Sci.* **116** 18233
[2] Rygg J R *et al* 2014 *Phys. Rev. Lett.* **112** 195001
[3] Tommasini R *et al* 2017 *Phys. Plasmas* **24** 053104
[4] Albert F *et al* 2013 *Phys. Rev. Lett.* **111** 1
[5] Lemos N *et al* 2024 *Phys. Rev. Res.* **6** L032022
[6] Corde S, Ta Phuoc K, Lambert G, Fitour R, Malka V, Rousse A, Beck A and Lefebvre E 2013 *Rev. Mod. Phys.* **85** 1
[7] Courtois C *et al* 2013 *Phys. Plasmas* **20** 083114
[8] Compant La Fontaine A, Courtois C, Gobet F, Hannachi F, Marquès J R, Tarisien M, Versteegen M and Bonnet T 2019 *Phys. Plasmas* **26** 113109
[9] Ta Phuoc K, Corde S, Thaury C, Malka V, Tafzi A, Goddet J P, Shah R C, Sebban S and Rousse A 2012 *Nat. Photon.* **6** 308
[10] Catravas P, Esarey E and Leemans W P 2001 *Meas. Sci. Technol.* **12** 1828
[11] Albert F *et al* 2017 *Phys. Rev. Lett.* **118** 134801
[12] Albert F, Pollock B B, Shaw J, Marsh K A, Ralph J E, Pak A, Clayton C E, Glenzer S H and Joshi C 2015 *Proc. SPIE* **9514** 72–81
[13] Joshi C, Tajima T, Dawson J M, Baldis H A and Ebrahim N A 1981 *Phys. Rev. Lett.* **47** 1285
[14] Najmudin Z *et al* 2003 *Phys. Plasmas* **10** 2071
[15] Mori W B, Decker C D, Hinkel D E and Katsouleas T 1994 *Phys. Rev. Lett.* **72** 1482
[16] Andreev N E, Gorbunov L M, Kirsanov V I, Pogosova A A and Ramazashvili R 1992 *JETP Letters* **55** 551
[17] Albert F *et al* 2018 *Phys. Plasmas* **25** 056706
[18] Edwards R D *et al* 2002 *Appl. Phys. Lett.* **80** 2129
[19] Li Y *et al* 2020 *High Energy Density Phys.* **37** 100859
[20] Shaw J L, Tsung F S, Vafaei-Najafabadi N, Marsh K A, Lemos N, Mori W B and Joshi C 2014 *Plasma Phys. Control. Fusion* **56** 084006
[21] Shaw J L, Lemos N, Amorim L D, Vafaei-Najafabadi N, Marsh K, Tsung F, Mori W B and Joshi C 2017 *Phys. Rev. Lett.* **118** 064801
[22] Esarey E, Shadwick B A, Catravas P and Leemans W P 2002 *Phys. Rev. E* **65** 15
[23] Wang S *et al* 2002 *Phys. Rev. Lett.* **88** 4
[24] Powers N D, Ghebregziabher I, Golovin G, Liu C, Chen S, Banerjee S, Zhang J and Umstadter D P 2014 *Nat. Photon.* **8** 28
[25] Pagano I M, Lemos N, King P M, Rusby D, Sinclair M, Aghedo A, Khan S, Downer M C, Joshi C and Albert F 2024 *Phys. Plasmas* **31** 073110

[26] Lemos N et al 2019 Phys. Plasmas 26 083110
[27] Lemos N et al 2018 Plasma Phys. Control. Fusion 60 054008
[28] Stoeckl C et al 2017 Phys. Plasmas 24 056304
[29] Samulski C, Srinivasan B, Manuel M J-E, Masti R, Sauppe J P and Kline J 2022 Matter Radiat. Extremes 7 026902
[30] Antonelli L et al 2024 Rev. Sci. Instrum. 95 113504
[31] Tommasini R et al 2008 Rev. Sci. Instrum. 79 10E901
[32] Lemos N, Marsh K A, Pollock B B, Tsung F S, Albert F, Joshi C, Shaw J L and Martins J L 2016 Plasma Phys. Control. Fusion 58 034018
[33] Fonseca R A et al 2002 Computational Science — ICCS 2002 ed P M A Sloot, A G Hoekstra, J K Tan and J J Dongarra (Springer) pp 342–51
[34] Shaw J L et al 2021 Sci. Rep. 11 7498
[35] Hansen A M, Haberberger D, Katz J, Mastrosimone D, Follett R K and Froula D H 2018 Rev. Sci. Instrum. 89 10C103
[36] McMillen K R, Heuer P V, Gjevre J M, Milder A L, Charles P, Filkins T, Rinderknecht H G, Froula D H and Shaw J L 2024 Rev. Sci. Instrum. 95 073517
[37] Dorrer C and Zuegel J D 2007 J. Opt. Soc. Am. B 24 1268
[38] Dorrer C, Consentino A and Irwin D 2016 Appl. Phys. B 122 156
[39] Mariscal D, Williams G J, Chen H, Ayers S, Lemos N, Kerr S and Ma T 2018 Rev. Sci. Instrum. 89 10I145
[40] Leblans P, Vandenbroucke D and Willems P 2011 Materials 4 1034
[41] von Seggern H 1999 Braz. J. Phys. 29 254
[42] Jackson Williams G, Maddox B R, Chen H, Kojima S and Millecchia M 2014 Rev. Sci. Instrum. 85 11
[43] Maddox B R, Park H S, Remington B A, Izumi N, Chen S, Chen C, Kimminau G, Ali Z, Haugh M J and Ma Q 2011 Rev. Sci. Instrum. 82 023111
[44] Moré J J and Sorensen D C 1983 SIAM J. Sci. Stat. Comput. 4 553
[45] Coleman T F and Li Y 1996 SIAM J. Optim. 6 418
[46] King P M et al 2020 Phys. Rev. Accelerators Beams 24 11302
[47] Zhang X, Khudik V N and Shvets G 2015 Phys. Rev. Lett. 114 184801
[48] Chen C D et al 2008 Rev. Sci. Instrum. 79 10E305
[49] King P M et al 2019 Rev. Sci. Instrum. 90 033503
[50] Virtanen P et al 2020 Nat. Methods 17 261
[51] Waggener R G, Blough M M, Terry J A, Chen D, Lee N E, Zhang S and McDavid W D 1999 Med. Phys. 26 1269
[52] Kneip S et al 2008 Phys. Rev. Lett. 100 105006
[53] Bullock A B, Landen O L and Bradley D K 2001 Rev. Sci. Instrum. 72 690
[54] Keiter P A and Workman J 2006 Rev. Sci. Instrum. 77 10E324
[55] Gotchev O V et al 2009 Phys. Rev. Lett. 103 215004
[56] Montgomery D S, Nobile A and Walsh P J 2004 Rev. Sci. Instrum. 75 3986
[57] Wood J C et al 2018 Sci. Rep. 8 1
[58] Barker L M and Hollenbach R E 1972 J. Appl. Phys. 43 4669
[59] Fourmaux S et al 2011 Opt. Lett. 36 2426
[60] Morace A et al 2014 Phys. Plasmas 21 102712
[61] Ravasio A et al 2010 Phys. Rev. E 82 016407